



On the Influence of Precipitation on the Dynamic Strain Aging in Mg-2%Nd

GERARDO GARCÉS ^{1,4} PABLO PÉREZ,¹ JUDIT MEDINA,¹
RAFAEL BAREA,² ADRIÁN GÓMEZ,³ JAVIER GARCÍA,³
and PALOMA ADEVA¹

1.—Department of Physical Metallurgy, National Center for Metallurgical Research, CENIM-CSIC, Avda. Gregorio del Amo 8, 28040 Madrid, Spain. 2.—Departamento de Ingeniería Industrial, Universidad Nebrija, Campus Dehesa de la Villa, C. Pirineos 55, 28040 Madrid, Spain. 3.—ICTS-National Center for Electron Microscopy UCM, Av. Complutense S/N, 28040 Madrid, Spain. 4.—e-mail: ggarces@cenim.csic.es

The Mg-2%Nd alloy, thermally treated at 520°C and quenched, exhibits plastic instabilities at intermediate temperatures between 100°C and 300°C when it is compressively tested because of the dynamic strain aging phenomenon caused by the presence of neodymium atoms in solid solution. During compression tests, there is a competition between the precipitation of Mg-Nd particles and the DSA phenomenon, which depends largely on the test temperature. Thus, below 200°C, the formation of neodymium-rich precipitates is slow, and the interaction is insignificant. Under these conditions, the alloy exhibits a normal behavior of the DSA, i.e., the critical strain decreases with the increase in the test temperature. However, for test temperatures > 200°C, the formation of neodymium-rich precipitates is faster and the evolution of the critical strain with temperature is inverted because of the decrease of neodymium in solid solution.

INTRODUCTION

Portevin–Le Chatelier (PLC) is a kind of dynamic strain aging (DSA) phenomenon caused by the interaction between solute (interstitial or substitutional) atoms and mobile dislocations.¹ This phenomenon has been referred to in many alloy systems: Al-based alloys, steels, Ti-based alloys, Ni-based alloys, Mg-based alloys, etc.^{2–13} For Mg-based alloys, the addition of rare earths has special influence on the appearance of this phenomenon at intermediate temperatures between 100°C and 250°C.^{14–23}

The DSA phenomenon is detected during the plastic flow, first because of the presence of a serrated behavior caused by the temporary locking of dislocations and twins by the solute atoms and, second, by the negative strain rate sensitivity (SRS).

The strain in which serrations begins in the deformation curve is defined as critical strain, ϵ_c , and depends strongly on the test temperature as well as the strain rate.²⁴ On one hand, the increase in the test temperature promotes solute atom diffusion. On the other hand, the increase in the strain rate raises the dislocations speed. As a result, the critical strain decreases with increase in test temperature or the decrease in strain rate. However, several studies reported this behavior in a low temperature range, but contrary behavior was shown at higher temperature, i.e., the critical strain increased with increases of the test temperature.^{9,25–27} Several reasons have been proposed to explain the inversion of the critical strain behavior: the presence of high-density stacking faults, the process by which dislocations break away from solute atoms or the simultaneous precipitation phenomenon at the same temperatures.

The Mg-Nd system exhibits a narrow solubility field. Thus, the maximum solubility of Nd in Mg is close to 3.5 wt.% at 552°C but drops to near zero for temperatures < 200°C, which provides a strong

(Received January 8, 2023; accepted March 13, 2023;
published online April 24, 2023)

potential for age hardening. The precipitation sequences of the Mg-Nd system have been widely described starting at low temperatures.^{28–32}

This paper studies the influence of precipitation on the DSA phenomenon in a Mg-2%Nd alloy during compression tests at intermediate temperatures. For this, the alloy was thermally treated to increase the solubility of neodymium in Mg to later be aged at different temperatures. The study has two parts; in the first, the precipitation reaction was followed by microhardness measurements. In the second, the microstructural evolution of the Mg-2%Nd alloy, in the as-thermal treatment condition, was studied during compression tests at different temperatures at different compressive strains to identify the deformation mechanism. Finally, the interaction between Nd atoms and Nd-rich precipitates with dislocations and twins was examined using transmission electron microscopy.

EXPERIMENTAL PROCEDURE

The alloy Mg-2%Nd (wt%) was fabricated using a casting route. High-purity Mg and a Mg-20%Nd (wt.%) master alloy were melted at 800°C in an electric resistance furnace and then cast in a steel mold. Analysis by ICP-OES technique indicates a composition of Mg-2.05% Nd in wt.%.

The cast cylinder of 42 mm diameter was homogenized and then extruded at 350°C with an extrusion ratio of 36:1. The extruded alloy was thermally treated at 525°C for 8 h (as-TT condition) buried in magnesium oxide to minimize oxidation and water quenched. Samples were aged at 150°C, 200°C and 250°C for different times. The aging process was followed by microhardness measurements applying a load of 200 g for 15 s in polished samples.

Compressive samples in the as-TT condition were tested along the extrusion direction in cylinders of 10 mm length and 5 mm diameter. Compressive tests were carried out at initial strain rate in the range of $4 \cdot 10^{-3}$ – $4 \cdot 10^{-5}$ s⁻¹ from room temperature to 300°C.

Scanning and transmission electron microscopy (SEM and TEM, respectively) and electron backscattered diffraction (EBSD) technique were used to characterize the microstructure of the alloy in the as-cast state, in the as-TT condition and after compression at different strain and aging states. Compression samples exhibit cylindrical symmetry where the perpendicular reference directions in micrographs and pole figures are: ED/LD (extrusion direction/load direction) and RD (radial direction). Notably, the load direction coincides with the extrusion axis before the solubilization treatment. Specimens for TEM after deformation were prepared by electrolytic polishing using a reactive mixture of 5.3 g lithium chloride, 11.2 g magnesium perchlorate, 500 ml methanol and 100 ml butoxy-ethanol at –50°C. Two transmission electron microscopes have been used in this study: a JEOL JEM 2100

microscope operating at 200 kV to analyze dislocation at twins at bright field and weak beam modes and a JEOL JEM 3000F microscope operating at 300 kV to analyze the formation of precipitation using the HAADF detector in the STEM mode.

The surface preparation of EBSD samples in magnesium alloys is delicate, and it is necessary to perform a final chemical etching in a solution of 7 ml acetic acid, 3 ml nitric acid, 30 ml ethanol and 10 ml water at 5°C submerging the sample 5 s.

Synchrotron diffraction patterns were analyzed in the annealed samples to investigate the presence and nature of precipitates on the P07B beamline of PETRA III (DESY, Hamburg, Germany). The diffraction patterns were recorded using an exposure time of 2 s and a Perkin-Elmer XRD 1622 flat panel detector with an array of 2048² pixel², with an effective pixel size of 200 × 200 μm². The wavelength of the beam was 0.014 nm. LaB₆ was used as a reference to calibrate the acquired diffraction spectra. The detector-to-sample distance was 2059 mm; 2θ diffraction patterns were obtained by azimuthal integration of the Debye–Scherrer rings along 360° using the FIT2D software.

RESULTS

Microstructure and Thermal Stability

Figure 1a shows the microstructure of the alloy in the as-cast condition consisting of the magnesium matrix and Mg₄₁Nd₅ phase located at the grain boundaries and within Mg grains. During extrusion process, the intermetallic phase is broken and aligned along the extrusion directions (Fig. 1b). The volume fraction of the second phase was estimated, and a value of 3.8% was obtained. Zhang et al.³³ have estimated the volume fraction of Mg₄₁Nd₅ intermetallic phase by experimental measurements and thermodynamic predictions. While the thermodynamic prediction indicates 4% of volume fraction very close to the value in this study, their experimental measurement was around 1%.

During the heat treatment at 525°C, only a partial solubilization of neodymium occurs and some equilibrium intermetallic phase remains (Fig. 1c). Figure 1d shows the orientation image mappings (OIMs) and the (0002) pole (Fig. 1e) figure of the alloy in this condition. The grain size is 187 μm, and grains are randomly oriented.

The effect of the precipitation on the mechanical strength at room temperature of the alloy has been evaluated measuring the microhardness variation. This information will be very useful to identify mechanical test temperatures where the precipitation process could interact with DSA phenomena. Figure 2 shows the evolution of hardness as a function of aging time at 150°C, 200°C and 250°C. The microhardness value of the alloy in the as-TT condition is 43. For the three aging temperatures, a hardness peak of around 63 is visible. The lower the aging temperature is, the higher the time required

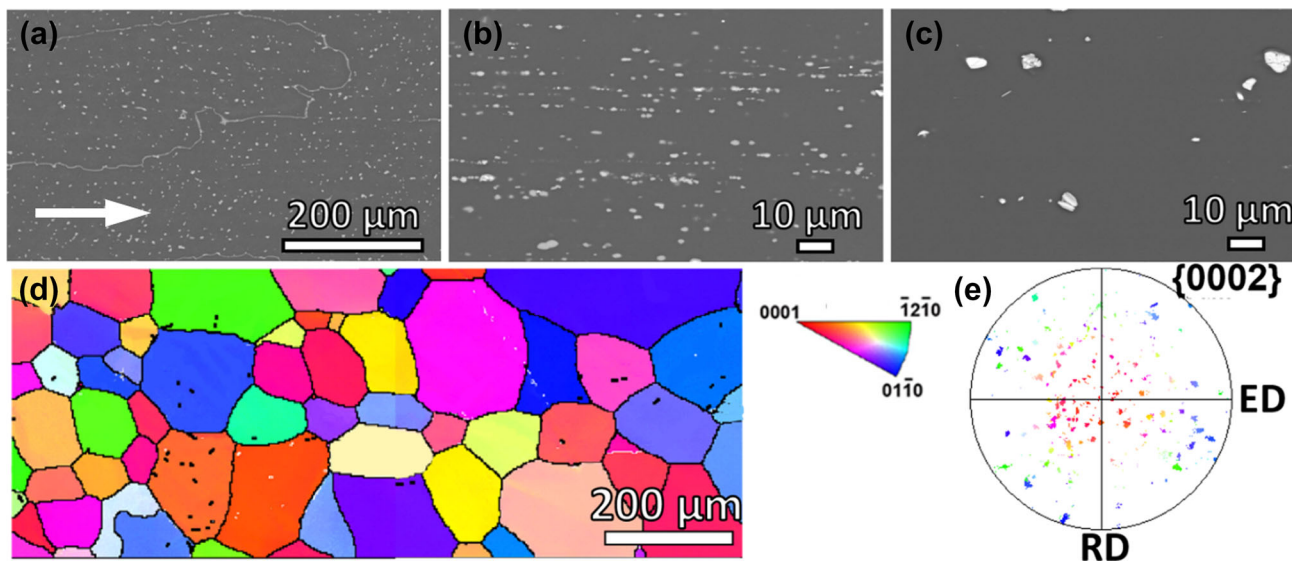


Fig. 1. SEM micrograph obtained in back-scattered electron (BSE) contrast showing the microstructure of the Mg-2%Nd. (a) as-cast condition, (b) extruded, (c) extruded and thermally treated 8 h at 525°C and quenched (as-TT condition). (d) Orientation image mapping (OIM) of the Mg-2%Nd alloy in the as-TT condition. (e) (0002) pole figures obtained from (d). Extrusion direction is indicated with the white arrow.

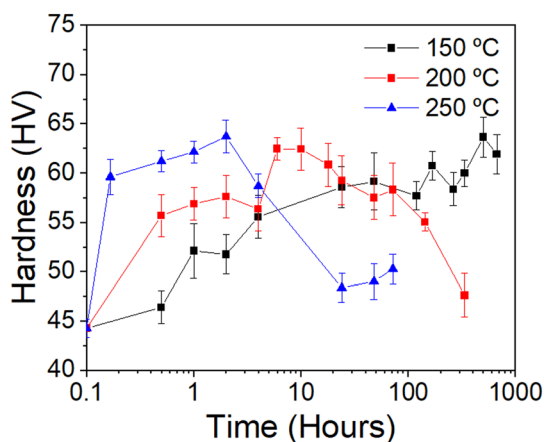


Fig. 2. Evolution of the Vickers microhardness of Mg-2%Nd alloy during aging at 150°C, 200°C and 250°C.

to reach the hardness peak. Notably, above 200°C, the hardness increases rapidly. At 200°C, the hardness value increases up to 56 after 30 min, and, at 250°C, the hardness value increases up to 60 after 10 min.

The precipitation phenomenon during the aging at 200°C has been followed using synchrotron diffraction at different aging times as well as by TEM, observing samples at the peak-aged (10 h) and over-aged (300 h) conditions. Figure 3 shows the diffraction pattern of the alloy aged at 200°C after different times. The diffraction peaks corresponding to the β_1 -Mg₃Nd phase appear after 72 h of aging, coinciding with the decrease in hardness observed in the curve, just after the peak. No additional peaks are observed for previous conditions.

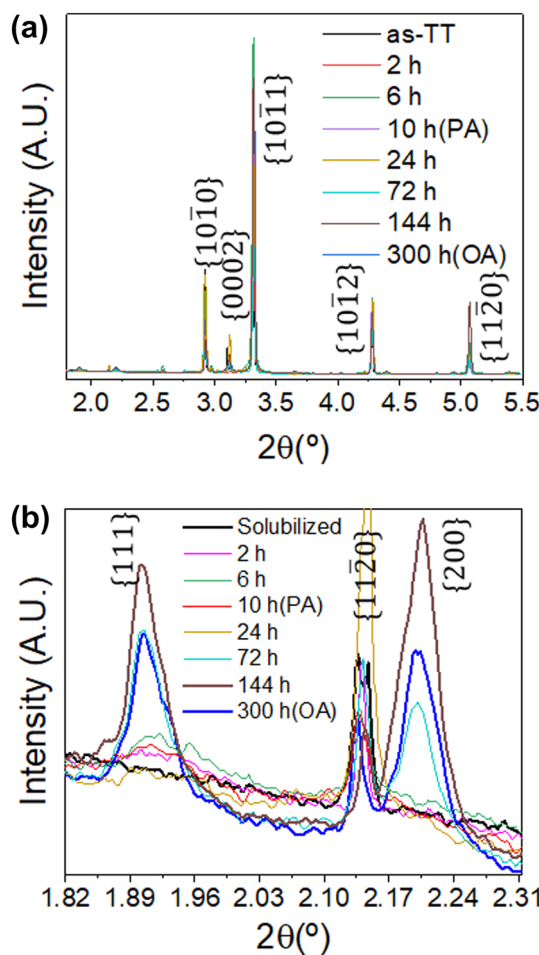


Fig. 3. Synchrotron diffraction patterns of the Mg-2%Nd alloy aged at 200°C at different aging times.

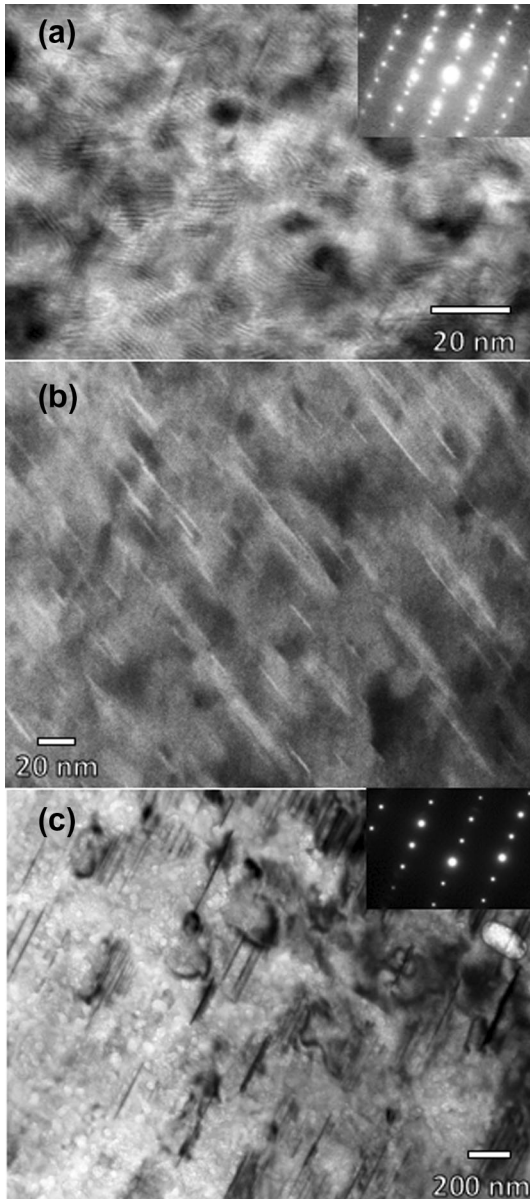


Fig. 4. (a–c) Mg-2%Nd alloy aged at 200°C in the peak-aged condition. (a) Bright-field TEM micrograph and SAED pattern, $B = [11\bar{2}0]$ zone axis; (b) DHAAF micrograph, $B = [11\bar{2}0]$ zone axis. (c) Bright-field TEM micrograph and SAED pattern $B = [11\bar{2}0]$ zone axis.

Figure 4a, b, and c shows bright-field micrographs of the alloy after 10 and 300 h of aging at 200°C in the zone axis $B = [11\bar{2}0]$. Small precipitates oriented along the $[0002]$ directions are observed. These precipitates, in the peak-aged conditions (10 h), are more clearly observed using the DHAAF detector (Fig. 4b) because of the higher neodymium concentration. The length of the precipitates increases from 10 or 20 nm under peak

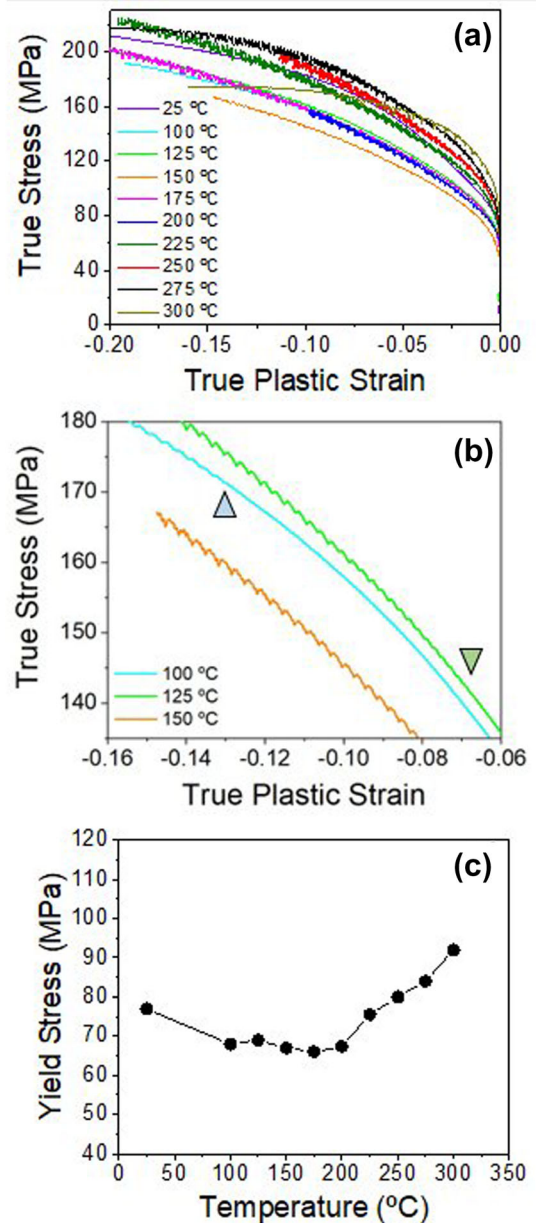


Fig. 5. (a, b) Compressive behavior of Mg-2%Nd alloy in the as-TT condition. (a) True stress-true strain curves at initial strain rate of 10^{-4} s^{-1} from room temperature to 300°C. (b) Detailed plot of (a) showing the serrated flow at 100°C, 125°C and 150°C. (The colored triangle shows the beginning of serrations at 100°C and 125°C). (c) Evolution of compressive yield stress from room temperature to 300°C.

aged condition to 200 nm under over-aging condition. Notably, diffuse streaks along $[10\bar{1}0]$ or $[11\bar{2}0]$ direction in the peak-aged condition are present that disappear completely in the over-aging state (Fig. 4c).

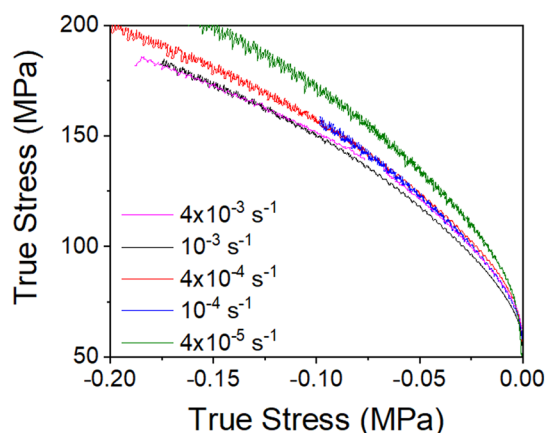


Fig. 6. True stress-true strain compressive curves of the Mg-2%Nd in the as-TT condition tested at 200°C at initial strain rates from 4.10^{-5} to 4.10^{-3} s^{-1} .

Mechanical Properties

Compressive tests at different temperatures between room temperature and 300°C at an initial strain rate of 10^{-4} s^{-1} of the alloy in the as-TT condition are shown in Fig. 5a. The true stress-true strain curves show that the alloy yields at a stress near 77 MPa and then greatly hardens continually during the plastic regime up to around 275°C (Fig. 5b). It is important to note the presence of the plastic instabilities (serrations) for temperature $> 100^\circ\text{C}$ (see details of Fig. 5b). The beginning of serration as well as the amplitude of these serrations depends on the test temperature. The compressive yield stress of the alloy in the as-TT condition slightly decreases with the increase in the test temperature up to 100°C (Fig. 5b). Then, it remains constant up to 200°C around 68 MPa; after that, it increases continuously with the increase in the compression temperature. This increase in the yield stress is directly related to the dynamic precipitation process during the compression test.

However, it has been demonstrated that the compressive behavior of the alloy in the as-TT condition is sensitive to the strain rate, as shown in Fig. 6. The curves correspond to the compressive behavior of the alloy at 200°C at different strain rates, and the stress and strain seem to increase with decreasing strain rate. The plastic strain at which the serration appears on the compression curve is defined as the critical strain, *critical strain*, ϵ_c .

The critical strain in the DSA phenomenon is generally described as a function the temperature and strain rate:^{34,35}

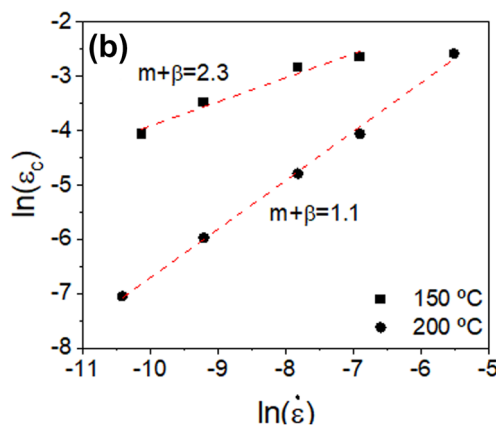
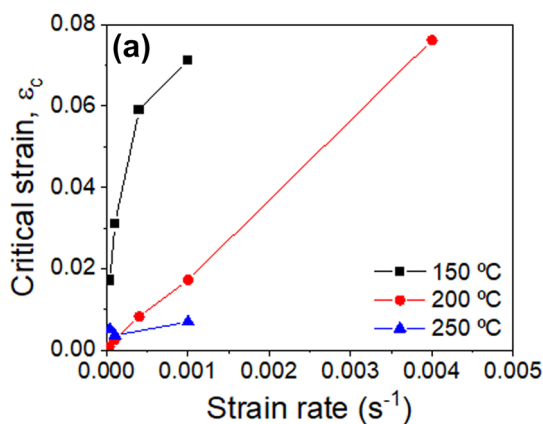


Fig. 7. (a, b) Mg-2%Nd in the as-TT condition tested in compression. (a) Evolution of the critical strain as a function of the initial strain rate tested at 150°C, 200°C and 250°C. (b) Logarithm of the critical stress as a function of the initial strain rate for compression at 150°C and 200°C.

$$\epsilon_c^{(m+\beta)} = K \cdot \dot{\epsilon} \cdot \exp\left(\frac{Q}{RT}\right) \quad (2)$$

where K , m and β are a constant, $\dot{\epsilon}$ is the strain rate, R is ideal gas constant, T is the temperature, and Q is the activation energy. Figure 7a shows the evolution of the critical strain as a function of the strain rate for compressive tests at 150°C, 200°C and 250°C. For 150°C and 200°C, the evolution of the critical strain follows the normal behavior in which the critical strain increases with the increase in the strain rate. However, at 250°C, the evolution of the critical strain shows an inverse behavior at low strain rates. The critical strain decreases from the strain rate from $4 \times 10^{-5} \text{ s}^{-1}$ to 10^{-4} s^{-1} , but then the critical strain returns to the normal increases from 10^{-4} s^{-1} to 10^{-3} s^{-1} . Figure 7b shows the evolution of the critical strain in logarithm scale as a function of the strain rate in temperature range

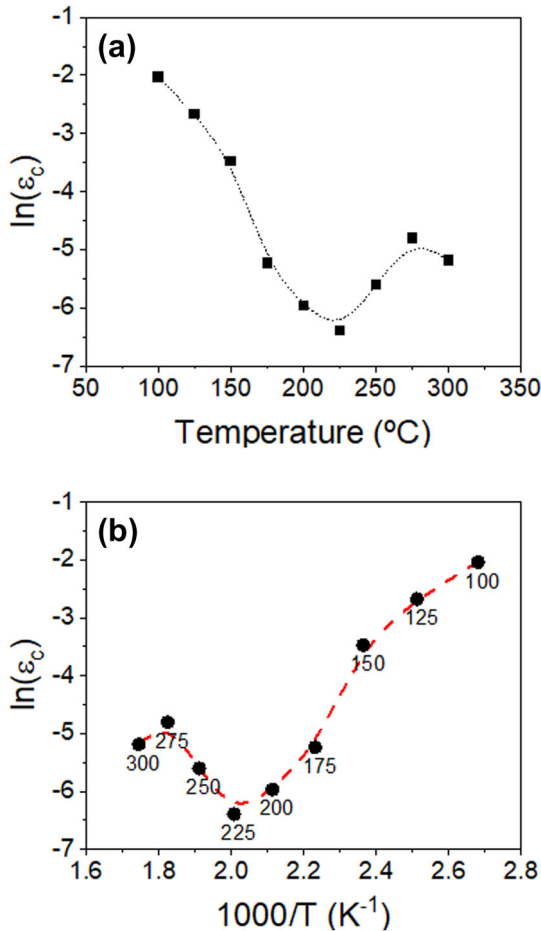


Fig. 8. (a, b) Mg-2%Nd in the as-TT condition tested in compression. Logarithm of the critical strain as a function of the (a) compressive temperature and (b) inverse of the compressive temperature.

in which normal behavior is observed. A linear behavior is obtained where the slope is the value of the constant $m + \beta$. Values are 2.3 and 1.1 at 150°C and 200°C, respectively.

The evolution of the critical strain as a function of the compression temperatures at 10^{-4} s^{-1} is presented in Fig. 8a. From 100°C to 225°C, the critical strain follows a normal behavior in which it decreases with the increase in the test temperature. However, above this temperature, the critical strain increases again up to 275°C. Finally, at 300°C, the critical strain decreases slightly with respect to 275°C. This wavy behavior has been reported previously by Brechet and Estrin.²⁷ Figure 8b shows the evolution of the critical strain in logarithmic scale as a function of the $1/T$. When the DSA phenomenon shows a normal behavior, it is expected to show a linear behavior where the slope is proportional to the activation energy given by:

$$\frac{Q}{(m + \beta) \times R} \quad (3)$$

It is not possible to obtain a general unique value for the activation energy for all studied temperatures since the variation of the constant $m + \beta$ is a function of temperature (see Fig. 7). A relative activation energy can be estimated calculating this value in two separated temperature ranges, 100–150°C and 175–225°C, using the values reported before. The activation energy is 85 and 48 kJmol^{-1} , respectively, for 100–150°C and 175–225°C.

Evolution of Deformed Microstructure

To understand the inverse behavior of the DSA phenomenon observed above 225°C, the microstructure of the deformed samples at different macroscopic strains has been characterized using SEM and TEM.

Figure 9a, b, c, d, e, f, g, h, I, j, k, and l shows the evolution of the orientation image mappings (OIMs) of the magnesium grains after strains of 2, 6 and 15% (at the end of the tests) at 100°C, 150°C, 200°C and 250°C at 10^{-4} s^{-1} using EBSD. After compression, twins are clearly observed within the magnesium grains. The twin volume fraction increases with the increase in the compression strain for all temperatures. However, the twin volume fraction decreases as the test temperature increases from 100°C to 250°C. As the compression strain increases, deformation and orientation gradients within magnesium grains are observed, even in those grains where twins are generated. These grain zones with small changes in the lattice orientation are developed by the accumulation of dislocations due to their continuous slip. This accumulation of dislocations induces the formation of low angle boundaries (white lines in Fig. 10) that develop inside grains after high deformation (around 15%), which are indicative of subgrain formation. These low-angle grain boundaries are mainly observed in grains oriented with the $\langle 10\bar{1}0 \rangle$ direction parallel to the normal direction of the micrograph. The texture of these grains suggests that they are completely twinned.

TEM samples were prepared after plastic deformation under two temperature conditions, 150°C and 250°C, and at strain rate of 10^{-4} s^{-1} to analyze the deformed microstructure of the sample in both DSA cases, normal behavior (100–225°C) and inverted behavior (225–275°C). Figure 11a and b shows the weak-beam dark field micrograph $B = [11\bar{2}0]$ zone axis of the alloy deformed at 150°C up to 2% of strain when the diffractions are $g = [10\bar{1}1]$ or $[0002]$. Dislocations are observed within the magnesium grains in all conditions. Therefore, the presence of $\langle a \rangle$ -type dislocations

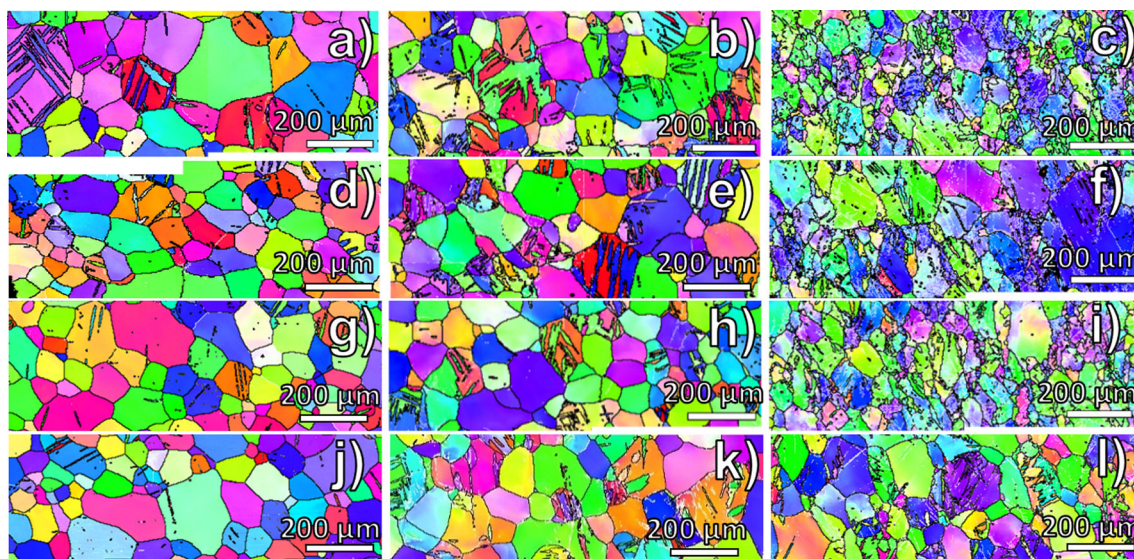


Fig. 9. (a–l) Orientation image mapping (OIM) of Mg-2%Nd in the as-TT condition tested in compression at 10^{-4} s^{-1} and compressive strains of 2%, 6% and 15% for the Mg-2%Nd. (a, b, c) 100, (d, e, f) 150, (g, h, i) 200 and (j, k, l) 250°C.

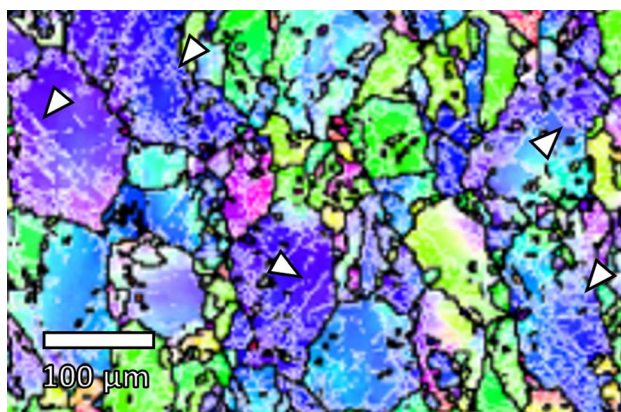


Fig. 10. Detail of the OIM of Mg-2%Nd in the as-TT condition tested in compression at 100°C at 10^{-4} s^{-1} deformed up to 15% of plastic strain.

which slip along the basal and non-basal planes and $\langle a + c \rangle$ -type dislocations which slip along the $\{11\bar{2}3\}$ planes is expected. Figure 11c and d shows the SAED patterns at the $B = [10\bar{1}0]$ and $B = [11\bar{2}0]$ zone axes, respectively. The presence of diffuse streaks along the $[10\bar{1}0]$ or $[11\bar{2}0]$ directions are not observed, in contrast to the micrograph in the peak-age condition already presented in Fig. 4a. Therefore, the formation of any coherent precipitates is not expected.

Figure 12a shows a bright micrograph of a twin in the grain of a $B = [11\bar{2}0]$ zone axis when the

diffraction vectors are $g = [0002]_m$ and $g = [10\bar{1}0]_t$. m and t refer to the matrix and twin, respectively. No dislocations are observed in the parent grain and outside twins under this diffraction g . However, when the diffraction vectors are $g = [10\bar{1}0]_m$ and $g = [0002]_t$ (Fig. 12c), a high density of straight dislocations parallel to the basal plane is observed. These dislocations have the $\langle a \rangle$ Burgers vector. On the other hand, inside twins, a high density of stacking faults throughout the twin width is observed when $g = [0002]_t$. These I_2 basal stacking faults are reported during plastic deformation, creep and thermal treatments in magnesium alloys.^{36–38} Tomsett and Bevis³⁹ and Wang and Agnew⁴⁰ also reported that I_2 basal stacking faults result from the transmutation process of $\langle a \rangle$ dislocation into $\langle c + a \rangle$ dislocation within the twins. Transmuted $\langle c + a \rangle$ dislocation is decomposed into $a \langle c \rangle$ dislocation and two Shockley $1/3 \langle 1\bar{1}00 \rangle$ dislocations (I_2 basal stacking faults).

Figure 13a and b shows the bright-field micrographs at the $B = [10\bar{1}1]$ and $B = [11\bar{2}0]$ zone axis of the alloy deformed at 250°C up to 2% of strain when the diffraction vector is $g = [10\bar{1}1]$ in both cases. Like the case of the alloy deformed at lower temperatures, dislocations are observed within the magnesium grains. Notably, dislocations exhibit a wavy shape which can be related with the strong interaction with small precipitates. This assumption is supported by the diffuse streaks observed in the SAED patterns along $[10\bar{1}0]$ or $[11\bar{2}0]$ direction

obtained in the $[10\bar{1}1]$, $[10\bar{1}0]$ and $[11\bar{2}0]$ zone axes (Fig. 13c–e), like those observed in the peak-aged conditions. Figure 13 shows the nanosize Nd-rich precipitates using the DHAAF detector in the $[11\bar{2}0]$ zone axes (Fig. 13f).

On the other hand, Fig. 14a shows a bright-field micrograph of a twin formed inside a magnesium grain of the sample deformed at 250°C up to 2% obtained in the zone axis $B = [11\bar{2}0]$. Similar to the materials deformed at low temperature, a high density of stacking faults throughout the twin width parallel to the basal plane is observed when the diffraction vectors are $g = [0002]_f$ (Fig. 14a). However, notably, small precipitates located in the twin boundaries form (Fig. 14b). Using the DHAAF detector, it is possible to see nanosized Nd-rich precipitates not only in the magnesium grains but also at the twin boundaries (Fig. 14c and d).

DISCUSSION

The thermal treatment of the extruded Mg-2%Nd at 525°C produces a partial solubilization of neodymium atoms within the magnesium matrix. Because the alloy is out of equilibrium, the precipitation of the Mg-Nd phases takes place following a complex sequence described in several papers.^{28–32} The early stage of the solid solution decomposition of these alloys results in the formation of Guinier–Preston (GP) zones that consist of zig-zag neodymium rows with a N, V or hexagonal shape. The hexagonal GP-rods are commonly defined as β'' and exhibit a $D0_{19}$ lattice structure. The next step corresponds to a mixture of two phases formed by combining the β' -Mg₇Nd (orthorhombic structure $a = 0.64$ nm, $b = 1.1$ nm, and $c = 0.52$ nm) ordering with the hexagons GP β'' . This precipitate mixture has been recently defined as β''' . Upon further aging, β_1 -Mg₃Nd (face-centered cubic structure, $a = 0.74$ nm) and β -Mg₁₂Nd (body-centered tetragonal phase $a = 1.031$ nm and $c = 0.593$ nm) metastable phases are developed. The β_1 -Mg₃Nd phase was observed for longer times in the aging treatments carried out at 200°C and 250°C (see Figs. 3 and 4). Finally, the equilibrium phase is the β_e -Mg₄₁Nd₅ (tetragonal structure, $a = 1.469$ nm and $c = 1.045$ nm), which was observed in the cast alloy as well as in the TT condition.

In this study we observed that the aging of the alloy induced an increase in the hardness value in the temperature range studied in the DSA phenomenon. The hardness peak is related with the formation of a network of the long-lasting GP-zones decorated by the β' -precipitates. Some authors have defined this mixed precipitation condition as β''' .³²

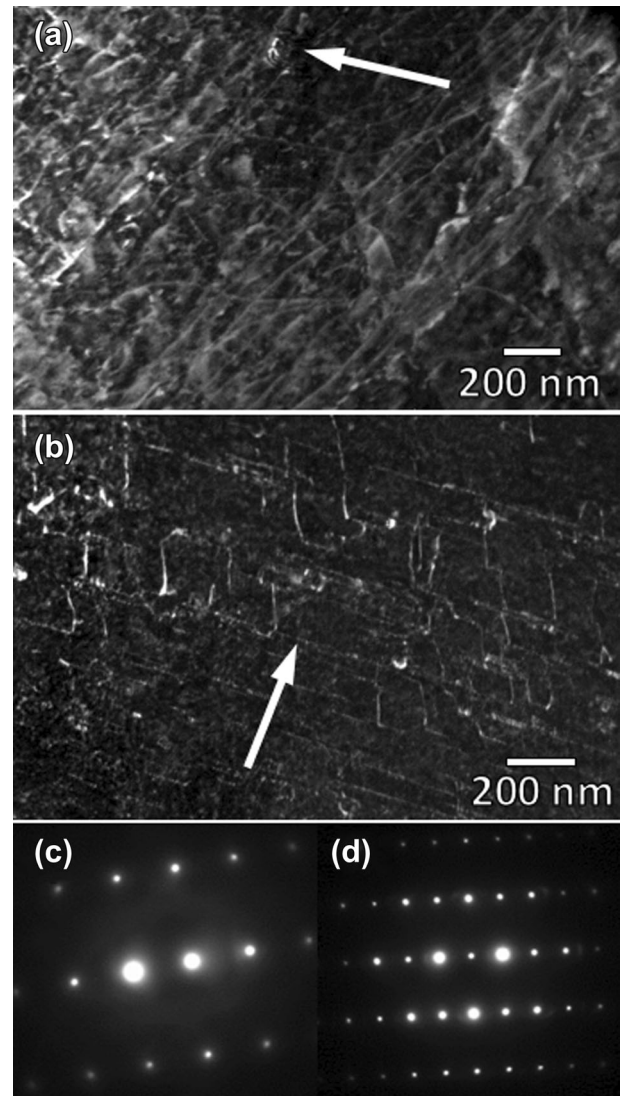


Fig. 11. (a–c) Weak beam TEM micrographs and SAED patterns of the Mg-2%Nd alloy in the as-TT condition tested in compression up to 2% of plastic deformation at 150 °C. (a) $B = [11\bar{2}0]$ zone axis, $10\bar{1}1$ g vector, (b) $B = [11\bar{2}0]$ zone axis, 0002 g vector, (c) $B = [10\bar{1}0]$ zone axis and (d) $B = [11\bar{2}0]$ zone axis.

Therefore, the precipitation reaction is interacting with the DSA phenomenon in two different directions. On one hand, the formation of neodymium-rich precipitates decreases the quantity in solid solution of neodymium atoms. Therefore, there are fewer solute atoms that can diffuse to lock temporary dislocations and twins. On the other hand, the heterogeneous nucleation of precipitates on dislocations or twins delays their movements and

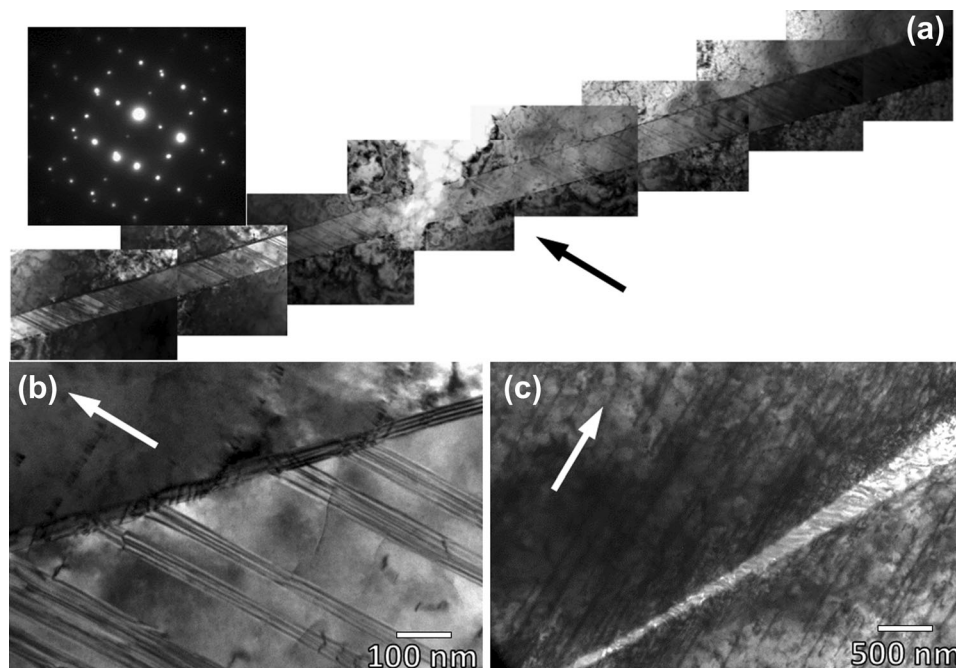


Fig. 12. (a) Bright-field TEM micrograph and SAED pattern of the Mg-2%Nd alloy in the as-TT condition tested in compression up to 2% of plastic deformation at 150°C. $B = [1120]$ zone axis, 0002 g vector; (b) detail of (a), 0002 g vector; (c) detail of (a) 1010 g vector.

facilities the diffusion of neodymium to lock them temporarily. This competition between precipitation and DSA depends strongly on the test temperature.

Below 200°C, the yield stress remained constant. From this temperature up to 300°C, the yield stress increased continuously up to a higher value than at room temperature, even because the test temperature increased. It would be expected that yield stress decreases continuously with the test temperature as it does in most magnesium alloys. Therefore, the precipitation phenomenon caused this in situ hardening of the alloys. At low temperatures, precipitation of neodymium-rich precipitates is also occurring, especially in GP zones. However, the time required for their formation is much longer than the time used to perform the compression test. Thus, the alloy aged at 150°C showed a hardness peak, but it took an hour of annealing at least to increase the hardness slightly. However, during the compression test at 150°C of the alloy in the as-TT condition, the presence of precipitates interaction with both dislocations and twins was not observed, as was presented at 250°C.

The precipitation phenomenon explains the inversion of the DSA behavior for temperatures $> 200^\circ\text{C}$. The homogeneous precipitation of β''' reduces the content of neodymium solute atoms in the magnesium matrix that can lock dislocations and twins. The exponent of the critical strain also showed a different value as the compression temperature in the normal behavior zone. At low temperature, the $m + \beta$ value is similar to that observed in other Mg-RE alloys,¹⁴⁻²³ which is between 3 and 2. However, at high temperature, when precipitation interacts with the DSA phenomenon, that value decreases to a value near 1. The initial model proposed by McCormick,²⁴ in which DSA is controlled by vacancies produced during deformation, associates constant parameters m and β with the quantification of vacancy and dislocation generation, respectively. However, more recent studies³⁵ propose that the mechanism that controls the strain aging is the solute diffusion along forest dislocation pipes, which intersect the mobile dislocation segment. In that case, β still defines the rate of increase in density of both mobile and forest dislocation

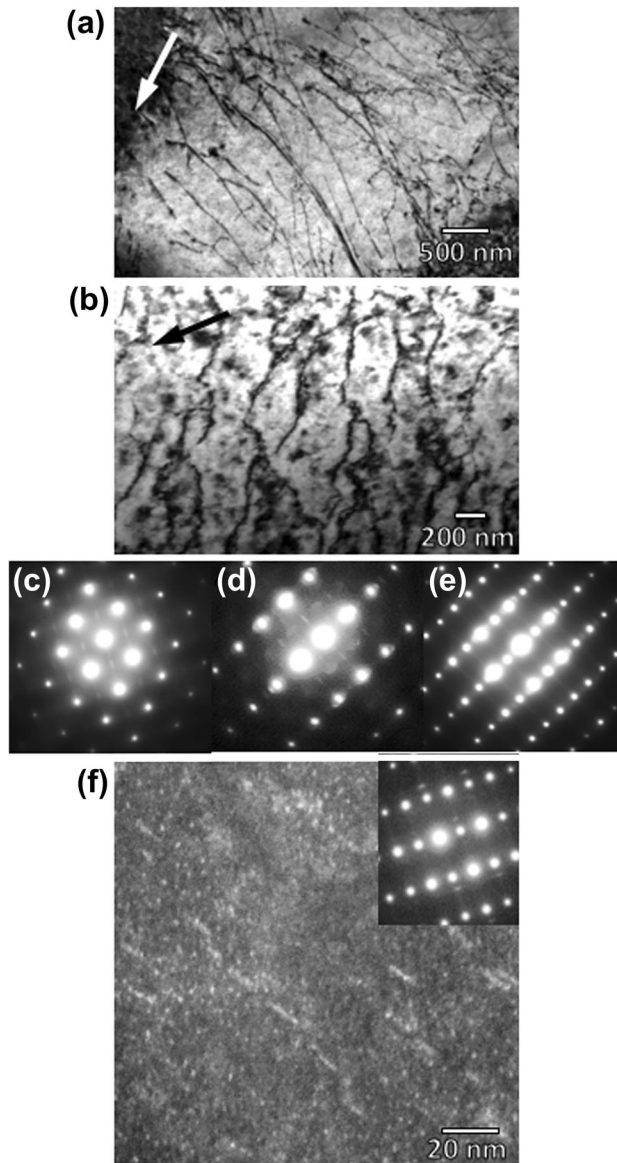


Fig. 13. (a–f) Bright-field TEM micrograph of the Mg-2%Nd alloy in the as-TT condition tested in compression up to 2% of plastic deformation at 250 °C at the (a) $B = [10\bar{1}1]$ and (b) $B = [11\bar{2}0]$ zones axes ($10\bar{1}1$ g vectors). SAED patterns obtained at (c) $B = [10\bar{1}1]$, (d) $B = [10\bar{1}0]$, (e) $B = [11\bar{2}0]$ zone axis. (f) DHAADF micrograph and SAED pattern, $B = [11\bar{2}0]$ zone axis.

segments but m has no clear meaning. In any case, the decrease in both constants near 1 is rarely reported in magnesium alloys. In the Mg-10%Ag alloy, Chaturvedi and Lloyd⁴¹ obtained values of

$m + \beta$ between 1.36 and 1.58. Authors proposed that these low values are due to the activation of only the basal slip system. However, the TEM analysis in this study has showed that non-basal slip system as well as tensile twinning is activated at intermediate temperature. On the other hand, Chavez et al.⁴² obtained values near 1 and proposed that these values are connected with the activation of the twinning system. EBSD maps indicated the activation of tensile twinning. However, the volume fraction of twins decreases with the increase of the compression temperature. Therefore, the decreases in the $m + \beta$ values could be connected with the decreases in the solute concentration in the magnesium matrix.

For temperature $> 200^\circ\text{C}$, the formation of neodymium-rich precipitates is faster and solute concentration is lower than at lower compression temperatures causing an increase in the critical strain because of the enhancement of diffusion of neodymium atoms. This fact causes the inverse behavior of the critical strain.

CONCLUSION

The influence of precipitation on the DSA phenomenon in the as-TT Mg-2%Nd alloy has been studied during compression tests at intermediate temperatures by a detailed analysis of the microstructure in the deformed samples. The following conclusions have been drawn:

1. The alloy in the as-TT condition exhibits flow serrations under compression tests in the temperature range of 100–300 °C. These plastic instabilities are associated with the DSA phenomenon because of the interaction of neodymium atoms with dislocations and twins.
2. The precipitation of GP zones and β''' takes place during the compression tests at intermediate temperature, which induces a hardening of the alloy above 200°C. Above this temperature, the precipitates also nucleate at dislocations and twin boundaries.
3. Below 200°C, the onset of the serrated flow (critical strain) in the alloy showed normal behavior such that the critical strain decreases with increasing compression temperature or decreasing strain rate. However, above 200°C, this behavior is reversed because of the precipitation of neodymium-rich precipitates, which decreases the number of neodymium atoms dissolved in the Mg matrix available to participate in the blocking phenomenon.

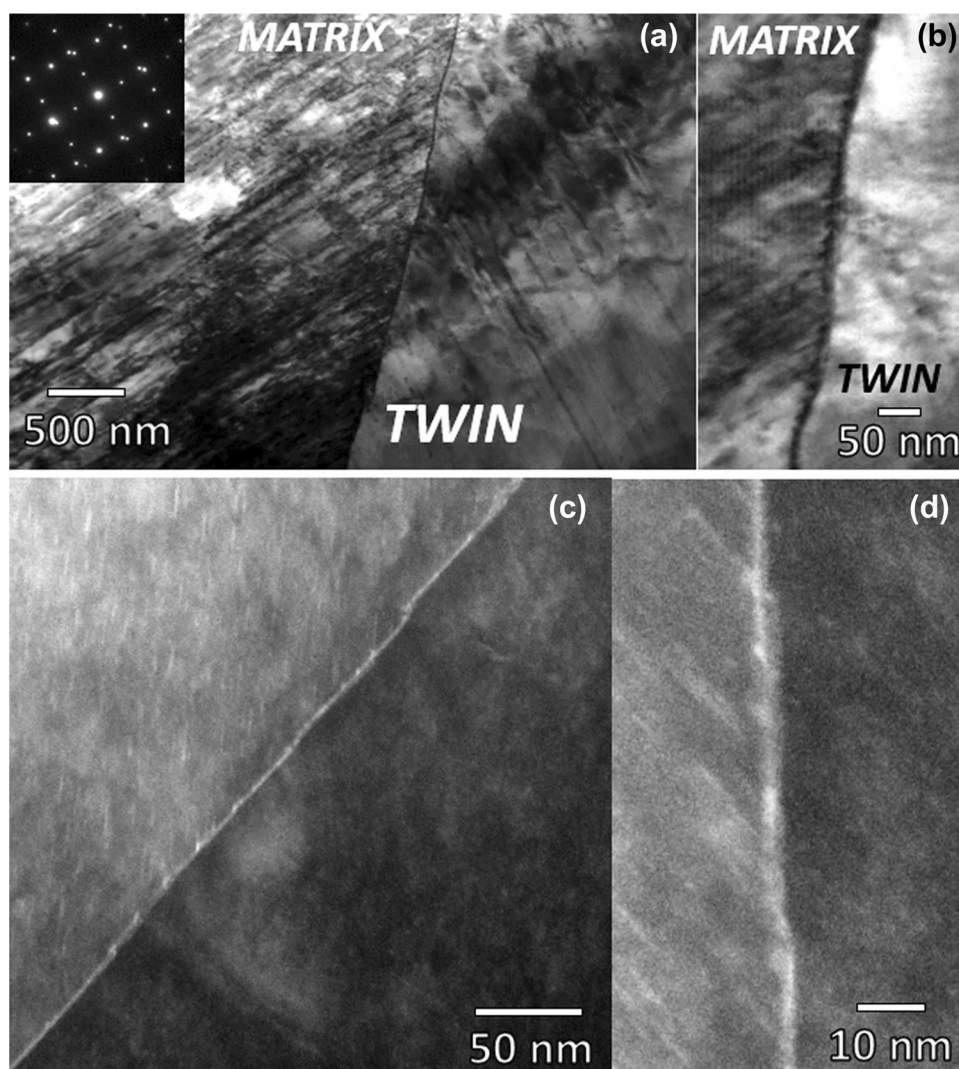


Fig. 14. (a) Bright-field TEM micrograph and SAED pattern of Mg-2%Nd alloy in the as-TT condition tested in compression up to 2% of plastic deformation at 250°C at the $B = [11\bar{2}0]$ zones axis. (b) Detail of the twin boundary. (c) DHAAF micrograph and SAED pattern, $B = [11\bar{2}0]$ zone axis. (d) Detail of the twin boundary.

ACKNOWLEDGEMENTS

We acknowledge the financial support of the Spanish Ministry of Economy and Competitiveness under project number TED2021-129580B-100. The Deutsches Elektronen Synchrotron DESY is acknowledged for the provision of beamtime at the P07B beamline of the PETRA III synchrotron radiation facility. Authors have no financial relationship with the organization that sponsored the research.

FUNDING

Open Access funding provided thanks to the CRUE-CSIC agreement with Springer Nature.

CONFLICT OF INTEREST

On behalf of all authors, the corresponding author states that there is no conflict of interest.

OPEN ACCESS

This article is licensed under a Creative Commons Attribution 4.0 International License, which permits use, sharing, adaptation, distribution and reproduction in any medium or format, as long as you give appropriate credit to the original author(s) and the source, provide a link to the Creative Commons licence, and indicate if changes were made. The images or other third party material in this article are included in the article's Creative Commons licence, unless indicated otherwise in a credit line to the material. If material is not included in the article's Creative Commons licence and your intended use is not permitted by statutory regulation or exceeds the permitted use, you will need to obtain permission directly from the copyright holder. To view a copy of this licence, visit <http://creativecommons.org/licenses/by/4.0/>.

REFERENCES

- J.M. Robinson, and M.P. Shaw, *Int. Mater. Rev.* 39, 113 <https://doi.org/10.1179/imr.1994.39.3.113> (1994).
- S. Zhang, Y. Estrin, and P.G. McCormick, *Acta Mater.* 49, 1087 [https://doi.org/10.1016/S1359-6454\(00\)00380-3](https://doi.org/10.1016/S1359-6454(00)00380-3) (2001).
- R.C. Picu, G. Vincze, F. Ozturk, J.J. Gracio, F. Barlat, and A.M. Maniatty, *Mater. Sci. Eng. A* 390, 334 <https://doi.org/10.1016/j.msea.2004.08.029> (2005).
- C. Wang, Y. Xu, and E. Han, *Mater. Lett.* 60, 2944 <https://doi.org/10.1016/j.matlet.2006.02.093> (2006).
- P. Verma, G. Sudhakar Rao, P. Chellapandi, G.S. Mahobia, K. Chattopadhyay, N.C. Santhi Srinivas, and V. Singh, *Mater. Sci. Eng. A* 621, 39 <https://doi.org/10.1016/j.msea.2014.10.011> (2015).
- B.K. Choudhary, *Mater. Sci. Eng. A* 564, 303 <https://doi.org/10.1016/j.msea.2012.11.104> (2013).
- S.S. Panwar, K. Prasad, T. Umasankar Patro, K. Balasubramanian, and B. Venkataraman, *Mater. Sci. Eng. A* 620, 286 <https://doi.org/10.1016/j.msea.2014.10.016> (2015).
- T. Sakthivel, K. Laha, M. Nandagopal, K.S. Chandravathi, P. Parameswaran, S. Panneer Selvi, M.D. Mathew, and S.K. Mannan, *Mater. Sci. Eng. A* 534, 580 <https://doi.org/10.1016/j.msea.2011.12.011> (2012).
- C.Y. Cui, Y.F. Gu, Y. Yuan, and H. Harada, *Scr. Mater.* 64, 502 <https://doi.org/10.1016/j.scriptamat.2010.11.025> (2011).
- K. Prasad, R. Sarkar, P. Ghosal, and V. Kumar, *Mater. Des.* 32, 1710 <https://doi.org/10.1016/j.matdes.2010.08.044> (2011).
- P. Agrawala, S. Karthikeyan, S.K. Makineni, B. Gault, and D. Banerjee, *Acta Mater.* 222, 117436 <https://doi.org/10.1016/j.actamat.2021.117436> (2022).
- S.L. Couling, *Acta Metall.* 7, 133 [https://doi.org/10.1016/0016-1600\(59\)90121-X](https://doi.org/10.1016/0016-1600(59)90121-X) (1959).
- M. Chaturvedi, D.J. Lloyd, and K. Tangri, *Met. Sci. J.* 6, 16 <https://doi.org/10.1179/030634572790446163> (1972).
- S.M. Zhu, and J.F. Nie, *Scr. Mater.* 50, 51 <https://doi.org/10.1016/j.scriptamat.2003.09.039> (2004).
- L. Gao, R.S. Chen, E.H. Han, Characterization of dynamic strain ageing in Mg-3.11wt.% Gd alloy, R.A. Nyberg, S.R. Agnew, N.R. Neelameggham, M.O. Pekguleryuz (Eds.), Annual conference of TMS (The Minerals, Metals & Materials Society), TMS, San Francisco, USA, 269, (2009).
- X.Y. Fang, D.Q. Yi, and J.F. Nie, *Metal Mater. Trans. A* 40, 2761 <https://doi.org/10.1007/s11661-009-9967-1> (2009).
- G. Garcés, M.A. Muñoz-Morris, D.G. Morris, P. Perez, and P. Adeva, *J. Mater. Sci.* 50, 5769 <https://doi.org/10.1007/s10853-015-9124-8> (2015).
- L. Jiang, J.J. Jonas, and R. Mishra, *Mater. Sci. Eng. A* 528, 6596 <https://doi.org/10.1016/j.msea.2011.05.027> (2011).
- N. Stanford, I. Sabirov, G. Sha, A. La Fontaine, S. Ringer, and M. Barnett, *Metall. Mater. Trans. A* 41, 734 <https://doi.org/10.1007/s11661-009-0107-8> (2010).
- D. Wu, R.S. Chen, and E.H. Han, *Mater. Sci. Eng. A* 532, 267 <https://doi.org/10.1016/j.msea.2011.10.090> (2012).
- W. Zhongjun, J. Weiping, and C. Jianzhong, *J. Rare Earths* 25, 744 [https://doi.org/10.1016/S1002-0721\(08\)60019-8](https://doi.org/10.1016/S1002-0721(08)60019-8) (2007).
- W.H. Wang, D. Wu, S.S.A. Shah, R.S. Chen, and C.S. Lou, *Mater. Sci. Eng. A* 649, 214 <https://doi.org/10.1016/j.msea.2015.09.100> (2016).
- V. Gärtnerová, Z. Trojanová, A. Jäger, and P. Palček, *J. Alloys Comp.* 378, 180 <https://doi.org/10.1016/j.jallcom.2003.11.172> (2004).
- P.G. McCormick, *Acta Metall.* 20, 351 [https://doi.org/10.1016/0001-6160\(72\)90028-4](https://doi.org/10.1016/0001-6160(72)90028-4) (1972).
- S.H. Fu, T. Cheng, and Q.C. Zhang, *Acta Mater.* 60, 6650 <https://doi.org/10.1016/j.actamat.2012.08.035> (2012).
- M.C. Cai, L.S. Niu, T. Yu, H.J. Shi, and X.F. Ma, *Mater. Sci. Eng. A* 527, 5175 <https://doi.org/10.1016/j.msea.2010.05.001> (2010).
- Y. Brechet, and Y. Estrin, *Acta Met. Mater.* 43, 955 [https://doi.org/10.1016/0956-7151\(94\)00334-E](https://doi.org/10.1016/0956-7151(94)00334-E) (1995).
- J.F. Nie, *Metal. Mater. Trans. A* 43, 3891 <https://doi.org/10.1007/s11661-012-1217-2> (2012).
- K. Saito, and K. Hiraga, *Mater. Trans.* 52, 1860 <https://doi.org/10.2320/matertrans.M2011163> (2011).
- A.R. Natarajan, E.L.S. Solomon, B. Puchal, E.A. Marquis, and A.V. Ven, *Acta Mater.* 108, 367 <https://doi.org/10.1016/j.actamat.2016.01.055> (2016).
- J.F. Nie, N.C. Wilson, Y.M. Zhu, and Z. Xu, *Acta Mater.* 106, 260 <https://doi.org/10.1016/j.actamat.2015.12.047> (2016).
- B. Zhou, L. Wang, B. Chen, Y. Jia, W. Wen, D. Li, D. Shu, P. Jin, X. Zeng, and W. Ding, *Mater. Sci. Eng. A* 708, 319 <https://doi.org/10.1016/j.msea.2017.10.011> (2017).
- Y. Zhang, Y. Huang, F. Feyerabend, C. Blawert, W. Gan, E. Maawad, S. You, S. Gavras, N. Scharnagl, J. Bode, C. Vogt, D. Zander, R. Willumeit-Römer, K.U. Kainer, and N. Hort, *Acta Biomater.* 121, 695 <https://doi.org/10.1016/j.actbio.2020.11.050> (2021).
- A.H. Cottrell, *Philos. Mag.* 74, 829 <https://doi.org/10.1080/14786440808520347> (1953).
- L.P. Kubin, and Y. Estrin, *Acta Metall. Mater.* 38, 697 [https://doi.org/10.1016/0956-7151\(90\)90021-8](https://doi.org/10.1016/0956-7151(90)90021-8) (1990).
- S. Morozumi, M. Kikuchi, and H. Yoshinaga, *Trans. JIM* 17, 158 <https://doi.org/10.2320/matertrans1960.17.158> (1976).
- S.Q. Zhu, and S.P. Ringer, *Acta Mater.* 44, 365 <https://doi.org/10.1016/j.actamat.2017.11.004> (2018).
- G. Garcés, J. Medina, P. Pérez, K. Máthis, K. Horváth, A. Stark, N. Schell, and P. Adeva, *Acta Mater.* 151, 271 <https://doi.org/10.1016/j.actamat.2018.03.060> (2018).
- D. Tomsett, and M. Bevis, *Philos. Mag.* 19, 533 <https://doi.org/10.1080/14786436908216310> (1969).
- F. Wang, and S.R. Agnew, *Int. J. Plast.* 81, 63 <https://doi.org/10.1016/j.ijplas.2016.01.012> (2016).
- M.C. Chaturvedi, and D.J. Lloyd, *Philos. Mag.* 30, 1199 <https://doi.org/10.1080/14786437408207276> (1974).
- B.W. Chávez, G. Garcés, P. Pérez, R. Barea, and P. Adeva, *Rev. Met.* 56, e175 <https://doi.org/10.3989/revmetalm.175> (2020).

Publisher's Note Springer Nature remains neutral with regard to jurisdictional claims in published maps and institutional affiliations.